

Drop bouncing by micro-grooves

V. Fink^a, X. Cai^{a,b}, A. Stroh^a, R. Bernard^{1,a}, J. Kriegseis^a, B. Frohnafel^a, H. Marschall^c, M. Wörner^{d,*}

^aKarlsruhe Institute of Technology (KIT), Institute of Fluid Mechanics, Kaiserstr. 10, 76131 Karlsruhe, Germany

^bKarlsruhe Institute of Technology (KIT), Institute for Chemical Technology and Polymer Chemistry, Engesserstr. 20, 76131 Karlsruhe, Germany

^cTechnische Universität Darmstadt, Mathematical Modeling and Analysis, Alarich-Weiss Str. 10, 64287 Darmstadt, Germany

^dKarlsruhe Institute of Technology (KIT), Institute of Catalysis Research and Technology, Engesserstr. 20, 76131 Karlsruhe, Germany

Abstract

Micro-textures are a well-known measure to increase surface hydrophobicity. Here, we experimentally investigate the impact of falling water droplets (diameter 2.1 mm, impact speed 0.62 m/s) on flat and structured surfaces made of the same hydrophobic material. While on the flat surface the drop settles with deposition, it bounces from the micro-grooved surface. Numerical simulations with a phase-field method mimicking the experiments do reproduce the different impact outcomes (deposition vs. bouncing) observed on both substrates. The axisymmetric simulations for the flat surface and the three-dimensional simulation for the structured surface employ the same grid size. In addition, the values for capillary width (chosen to be about 1% of the drop diameter) and mobility are the same in both simulations, where in the wetting boundary condition the static contact angle on the flat surface (100.3°) is identically used. Recovering the distinct experimental impingement outcomes in the simulation, though limited to one specific combination of drop diameter and impact speed, highlights the potential of the phase-field method for correctly predicting drop impact phenomena on flat and micro-structured surfaces under adequate resolution. Concerning the instantaneous droplet shape, the agreement between computations and experiments on both substrates is, however, only good till the beginning of the receding phases, whereas thereafter, significant differences are obtained.

Keywords: drop impact, deposition, rebound, structured hydrophobic surface, phase-field method, shadowgraphy

1. Introduction

Drop impact on a solid surface is a long-standing research topic since Worthington [1] performed first studies on this subject in 1876. Nowadays, the process can be recorded with a high-speed camera so that the drop deformation can be observed highly resolved in space and time. Due to its great practical importance in nature and a wide variety of industrial processes, the impact of a drop on a solid surface is intensively studied. The current status with emphasis on experiments is discussed in review papers by Yarin [2] and Josserand and Thoroddsen [3].

In recent years, the focus of studies on drop impact has changed from flat to structured surfaces, since modern fabrication techniques allow a precise micro-structuring of surface morphology [4] aiming to tune the surface wettability towards hydrophilicity or hy-

drophobicity [5, 6]. The morphology of the micro-structured surface may have a significant influence on the drop impact behaviour [7], similar to that for flat surfaces with different irregular roughness [8]. Micro-structuring a surface of a certain material, e.g., by grooves, can influence maximum spreading [9] and impact outcome [10], enhance the intensity of the drop rebound [11], and can both suppress and facilitate splashing dependent on surface morphology [12]. Furthermore, hydrophobic micro-patterning a surface can even cause a drop to rebound, when otherwise deposition occurs [7, 10, 13, 14]. Such a behaviour is of interest for several technical applications (e.g., self-cleaning and anti-icing) and is also observed in the present study.

In contrast to experiments, numerical studies on the impact of millimetre-size drops on spatially resolved structured surfaces are rare. Most studies use a two-dimensional approach either with lattice Boltzmann [15, 16] and phase-field [17] methods or by many-body dissipative particle dynamics [18, 19]. Only recently, full three-dimensional simulations on drop im-

*Corresponding author *E-mail address:* martin.woerner@kit.edu

¹present address: University of Stuttgart, Institute of Aerospace Thermodynamics, Pfaffenwaldring 31, 70569 Stuttgart, Germany

impact on structured surfaces using an advanced geometric volume-of-fluid method [20] and an entropic lattice Boltzmann method [21] became available. From these numerical studies, only few consider drop bouncing [15, 18, 19, 21].

In the present study, the vertical impact of a 2.1 mm water drop on a flat as well as on a structured horizontal surface made of the same hydrophobic material is investigated. Experiments with a high-speed camera reveal a quite different behaviour of the impacting droplet on the two surfaces. While on the flat surface the impact proceeds in deposition mode, the drop bounces from the substrate structured by micro-grooves before impacting a second time with subsequent deposition. Axisymmetric numerical simulations for the flat surface and full three-dimensional simulations for the structured surface based on the phase-field approach reproduce the distinct experimental impingement outcomes on both substrates, pointing to the potential of the method for predictive computations.

The paper is organized as follows. In Sections 2 and 3, the experimental and numerical methods are introduced. The results on the flat and structured surfaces are presented and discussed in Sections 4 and 5, respectively. Section 6 is devoted to summary and conclusions.

2. Experiment

For the experimental investigation of the impact process, the droplet shape is captured utilizing shadowgraphy technique [22]. Fig. 1 illustrates the set-up of the present experiment. A syringe with an inner dispense tip diameter of 0.1 mm is mounted 2 cm above the test surface. The syringe is used to generate single distilled water droplets. Driven by gravity, the droplets fall with a diameter of $D_0 = 2.1$ mm through the quiescent air and reach an impact velocity u_0 of 0.61 – 0.64 m/s. The drop is illuminated from the back and a high-speed camera "pco.1200 hs" records the shadow image of the impacting droplet with a 120/6 lens at a frame rate of 3200 fps and an exposure time of 15 μ s.

The drop impact on two different horizontal test surfaces is investigated. Both surfaces are made of hydrophobic polydimethylsiloxane (PDMS). The first surface is flat while the second one is structured with regular grooves as depicted in Fig. 2. The characteristic dimension of the grooved surface is given by $s = 60$ μ m. For the flat PDMS surface, the roughness has been measured. The mean roughness (Ra) is 0.078 μ m while the mean roughness depth (Rz) defined as the arithmetic

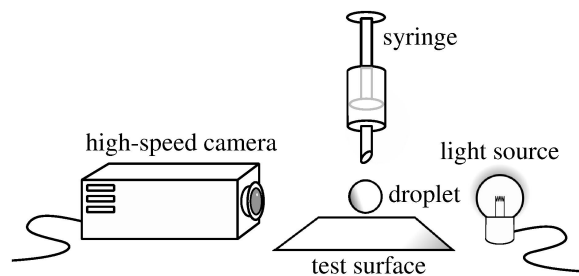


Figure 1: Schematic of the shadowgraphy set-up.

mean value of the single roughness depths of five consecutive sampling lengths is 0.56 μ m. The roughness of the ridges of the structured surface has not been measured but is expected to be similar so that the roughness depth would be about 1% of the groove dimension s .

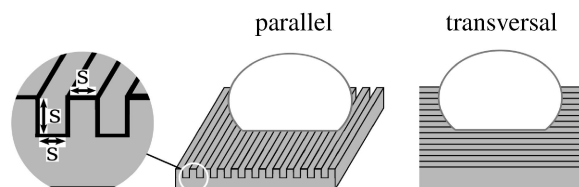


Figure 2: Geometry of the investigated surface structure (left, $s=60$ μ m) with camera perspectives directed parallel/longitudinal (middle) and transversal (right) to the grooves.

Since the wetting behaviour on the flat surface is assumed to be axisymmetric, the impact process is recorded from one side only. For the structured surface, the impact is investigated consecutively from two different orthogonal perspectives as illustrated in Fig. 2. In order to minimize the experimental uncertainty, the three experiments are repeated 20 times while the surface is cleaned with isopropyl after each iteration. Table 1 summarizes the average initial (before impact) drop diameter D_0 and impact velocity u_0 for each experiment along with the corresponding standard deviations. The uncertainties in the present work correspond to a 68.2% confidence interval. The impact velocity is determined based on the travelled distance of the droplet from the second last to the last image before impact.

surface	D_0 [mm]	u_0 [m/s]
flat	2.086 ± 0.004	0.6072 ± 0.0202
structured transversal	2.079 ± 0.007	0.6413 ± 0.0348
structured parallel	2.076 ± 0.005	0.6086 ± 0.0280

Table 1: Evaluated and averaged initial diameter D_0 and impact velocity u_0 with their standard deviations.

The physical properties of water and air are given in Table 2. The value of the Bond number is $Bo = g\rho_w D_0^2/\sigma \approx 0.59$ where $g = 9.81 \text{ m}^2/\text{s}$. Accordingly, surface tension forces predominate over gravity and the falling droplets can be considered as spheres which is confirmed by the recorded images. The values of the Reynolds and Weber numbers are $Re = \rho_w D_0 u_0/\mu_w \approx 1300$ and $We = \rho_w D_0 u_0^2/\sigma \approx 11$, respectively.

parameter	symbol	value	unit
water density	ρ_w	998.2	kg/m^3
water viscosity	μ_w	$1.005 \cdot 10^{-3}$	Pa s
air density	ρ_A	1.2	kg/m^3
air viscosity	μ_A	$1.55 \cdot 10^{-5}$	Pa s
surface tension	σ	$72.8 \cdot 10^{-3}$	N/m
contact angle	θ_{eq}	100.3	$^\circ$

Table 2: Fluid properties.

3. Numerical Simulation

3.1. Governing equations

The present simulations are performed by a phase-field method where the gas-liquid interface is considered as a thin transition layer of finite width [23]. The spatial distribution of the phases is described by an order parameter C . Here, C takes distinct values $C_w = 1$ and $C_A = -1$ in the liquid and gaseous bulk phases, respectively, and varies rapidly yet smoothly in a thin transition layer. The spatiotemporal evolution of the phase distribution is described by the convective Cahn-Hilliard equation

$$\frac{\partial C}{\partial t} + \nabla \cdot (C\mathbf{u}) = M\nabla^2\phi. \quad (1)$$

In the diffusive term on the right hand side of this equation, M denotes the mobility parameter and ϕ the chemical potential. The latter is defined as

$$\phi = \frac{\lambda}{\varepsilon^2} C(C^2 - 1) - \lambda\nabla^2 C. \quad (2)$$

Here, ε is a positive constant (denoted as capillary width) which determines the thickness of the diffuse interface. For a flat interface in equilibrium, the mixing energy density λ relates to ε and surface tension σ as

$$\lambda = \frac{3\sqrt{2}\sigma\varepsilon}{4}. \quad (3)$$

In the present study, σ and ε serve as input parameters for the simulations so that λ follows from Eq. (3). Following [24, 25], the mobility is specified as

$$M = \chi\varepsilon^2, \quad (4)$$

where χ is a constant pre-factor.

The immiscible two phase flow of water and air has to satisfy the condition for the velocity field, Eq. (5), and the single-field Navier-Stokes Eq. (6)

$$\nabla \cdot \mathbf{u} = 0, \quad (5)$$

$$\begin{aligned} \frac{\partial}{\partial t}(\rho_C\mathbf{u}) + \nabla \cdot (\rho_C\mathbf{u}\mathbf{u}) = \\ -\nabla p + \nabla \cdot (\mu_C(\nabla\mathbf{u} + \nabla\mathbf{u}^\top)) + \mathbf{f}_\sigma + \rho_C\mathbf{g}, \end{aligned} \quad (6)$$

where p is the pressure and \mathbf{g} the gravity vector.

The density and viscosity fields depend on the order parameter as

$$\rho_C = \frac{1+C}{2}\rho_w + \frac{1-C}{2}\rho_A, \quad (7)$$

$$\mu_C = \frac{1+C}{2}\mu_w + \frac{1-C}{2}\mu_A, \quad (8)$$

while the surface tension force is given by

$$\mathbf{f}_\sigma = -C\nabla\phi. \quad (9)$$

Equations (7) – (9) and the velocity field \mathbf{u} couple the Navier-Stokes Eq. (6) with the Cahn-Hilliard Eq. (1).

The above system of equations is solved numerically using a finite volume method in OpenFOAM®. For details on the numerical method, the solution algorithm of the underlying top-level solver *phaseFieldFoam*, and its validation, the reader is referred to [26, 27, 28, 29].

3.2. Numerical set-up

The numerical simulation is set-up to mimic the experimental conditions. In accordance with the above equations, water and air are treated as one effective mixture, consisting of two immiscible, incompressible, isothermal, and Newtonian fluids with the physical properties given in Table 2. The initial conditions, the boundary conditions at the solid wall, and the numerical parameters are identical for the flat and structured surface, whereas the domain size and other boundary conditions differ as indicated below.

3.2.1. Initial conditions

The experimentally determined values for D_0 and u_0 serve as input parameters for the initial conditions. In particular, the drop radius is set to $R_0 = D_0/2 = 1.05$ mm with an initial vertical positioning of its centre at R_0 above the surface so that the droplet is in point contact with the surface. At this location, the water droplet is initiated with a downward velocity of $u_0 = 0.62$ m/s in stagnating air. The distribution of the order parameter is smoothed near the interface according to the hyperbolic tangent profile of a flat interface in equilibrium.

3.2.2. Boundary conditions at the solid wall

An important aspect in the numerical simulation of drop impact phenomena is the adequate modelling of the moving contact lines that appear at the intersection between the gas, fluid, and solid phases. Here, the phase-field method has potential advantages as compared to sharp-interface methods (such as the geometric volume-of-fluid method and the level-set method) as the non-zero right-hand-side of the Cahn-Hilliard Eq. (1) provides a diffusive mechanism allowing the contact line to move at a no-slip wall.

In the phase-field method, the surface wettability can be represented by the energy equilibrium boundary condition for the order parameter

$$\partial_n C = \mathbf{n}_s \cdot \nabla C = \frac{\sqrt{2} \cos \theta_{\text{eq}}}{2} \frac{1 - C^2}{\varepsilon}, \quad (10)$$

where $\partial_n C$ denotes the surface normal gradient with \mathbf{n}_s being the outward unit normal to the solid surface [24]. In the present computations, the right-hand-side of Eq. (10) is treated explicitly. There, θ_{eq} could in principle be replaced by a dynamic contact angle model dependent on the contact line speed. However, using a constitutive relation for the dynamic contact angle is usually disregarded in the phase-field method because the competition between Cahn-Hilliard diffusion and convection already results in a bending of the interface in the vicinity of the wall. While by Eq. (10), the slope of the interface at the wall corresponds to θ_{eq} , the slope evaluated on a somewhat larger scale deviates from θ_{eq} , reflecting the dynamic contact angle of the hydrodynamic wetting theory of Cox's [30], see [31, 32].

3.2.3. Numerical parameters

Numerical parameters are chosen according to the experience gained by a preliminary feasibility study [33], where the influences of capillary width (ε), mobility (M), grid resolution (h), diffuse interface resolution

(h/ε), domain size and time step width has been investigated. In phase-field computations, the diffusive interface thickness (controlled by ε) is chosen much larger than the physical interface thickness in order to save computations costs. The value of ε is often determined by relating it to a macroscopic length scale, here the drop diameter. The value of the Cahn number $Cn = \varepsilon/D_0$ representing this ratio is typically chosen of order 0.01 or smaller. Here we use $Cn = 0.0105$ implying $\varepsilon = Cn \cdot D_0 = 22$ μm . The size of the uniform grid is set to $h = 10$ μm corresponding to a resolution of about nine cells for the diffuse interface (i.e., the distance 4.164ε where, for a planar interface, C varies from -0.9 to 0.9 at equilibrium). Accordingly, the initial drop diameter is resolved by 210 mesh cells.

A critical issue in the phase-field method is the specification of the mobility, respectively χ (cf. Eq. 4), since M is no documented physical property so far. In practice, χ is, therefore, often either determined by fitting experimental data, see e.g. [25, 28], or simply set to unity ($\chi = 1$ m·s/kg). Supported by results of our feasibility study [33], we here follow the latter approach so that $M = 4.84 \cdot 10^{-10}$ m³s/kg. For the flat surface, one additional simulation with the reduced value $\chi = 0.413$ m·s/kg is performed to illustrate the influence of the mobility ($M = 2 \cdot 10^{-10}$ m³s/kg). However, no attempt is made in this paper to improve the agreement between computational and experimental results by tuning the mobility. The analysis of the instantaneous droplet shapes is therefore based on simulation results obtained with the reference mobility ($\chi = 1$ m·s/kg).

The time step size is variable underlying a maximum Courant number limit in the range 0.03 – 0.05. While these values appear quite low, we remark that the present solver is based on a segregated solution of the Cahn-Hilliard and Navier-Stokes equations. A new solver with coupled solution is under development and we expect that this will allow for larger Courant numbers. For all presented simulations the mass loss of the liquid phase is less than 1% and the order parameter is always in the range $-1 \leq C \leq 1.03$.

3.2.4. Simulation domain for flat surface

The simulations for the drop impact on the flat surface are performed by a two-dimensional axisymmetric set-up where the computational domain has the shape of a wedge. The wedge has a width of $2.1R_0$, has a height of $3.1R_0$, and has an opening angle of 3.9° . Fig. 3 shows the computational domain in grey and its rotational extrusion with the droplet indicated in black. The wedge is meshed by 220×330 cells, resulting in 72,600 mesh cells in total.

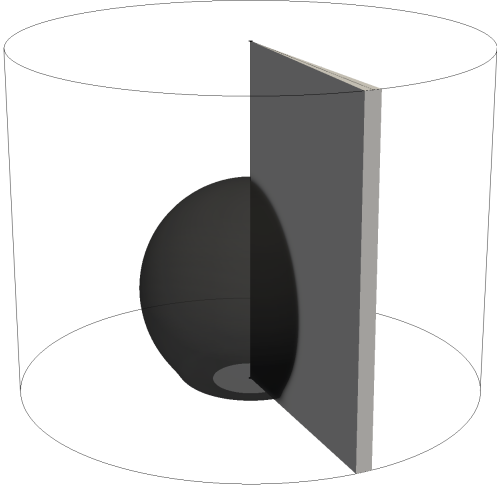


Figure 3: Sketch of the wedge (grey) representing the computation domain for the axisymmetric impact simulations of a drop (black, displayed not for the initial but a later time) on a flat surface.

The bottom of the wedge is defined as a no-slip wall with the wetting boundary condition given by Eq. (10), and the static (equilibrium) PDMS contact angle $\theta_{\text{eq}} = 100.3^\circ$. At the two lateral faces of the wedge, symmetric boundary conditions apply. The upper and outer radial faces of the wedge are free stream borders so that mass can enter and leave over both boundary patches in combination with a zero gradient condition for the order parameter. The time step size is of order $0.1 \mu\text{s}$ and the simulation runs till 100 ms.

3.2.5. Simulation domain for structured surface

In this case the numerical set-up has to capture the spherical drop impacting on the grooved structure. Therefore, the simulation domain needs to be three-dimensional. To limit computational time, we take advantage of the two vertical symmetry planes of the problem and consider one quarter of the drop only. Fig. 4 shows the computational domain in grey embedded in the full mirrored geometry. The dimension of the computational domain is 2 mm in direction of the grooves, 1.8 mm perpendicular to the grooves, and 5 mm in height corresponding to $1.9R_0 \times 1.7R_0 \times 4.8R_0$. The grid size $h = 10 \mu\text{m}$ corresponds to a resolution of the groove width and height s by 6×6 cells resulting in 18 million mesh cells in total for the entire computational domain.

The boundary conditions are chosen as in the flat case. The bottom is defined as no-slip wall with the wetting boundary condition given by Eq. (10). As the grooves are adequately resolved, the static contact angle of the flat PDMS surface is used again. At the two

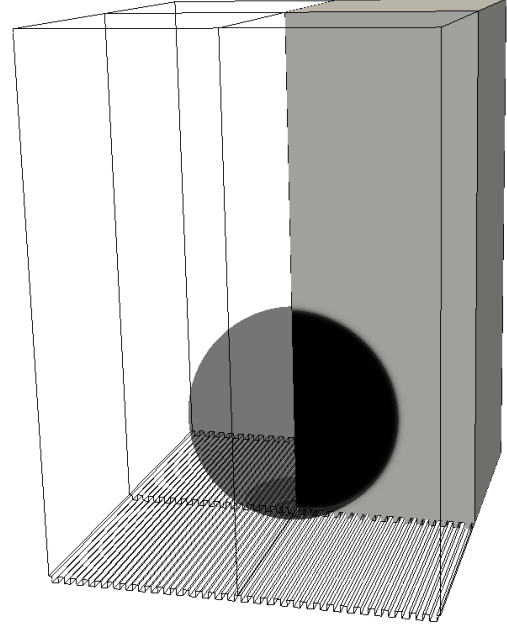


Figure 4: Sketch of the cuboid (grey) representing the computational domain for the three-dimensional impact simulations of a drop (black) on a surface structured by parallel grooves.

outer vertical faces of the computational domain, free stream boundary conditions apply, while at the two inner ones, symmetry boundary conditions are used. The time step size is of order $0.01 \mu\text{s}$ and the simulation runs till 117 ms. In order to provide reasonable time-to-solution, the solver is executed in parallel mode. Prior to the main simulation a scalability study with variation of CPU core number from 60 to 1000 is performed for the present computational domain. The study reveals a significant speed-up for the parallel computation up to 500 CPU cores. Based on this result and available computational resources, the final simulation is carried out on 500 CPU cores during 66 days (33 consecutive runs with 2 days runtime each). The total computational costs to run the simulation till 117 ms using a time step size of order $0.01 \mu\text{s}$ are approximately estimated to 800,000 CPUh.

4. Results for drop impact on flat surface

While the numerical data set provides the possibility to analyse full details of the internal flow within the droplet as discussed, e.g., in [34], the focus of the present paper is on comparison with the experiment, where data for the instantaneous phase distribution are available only.

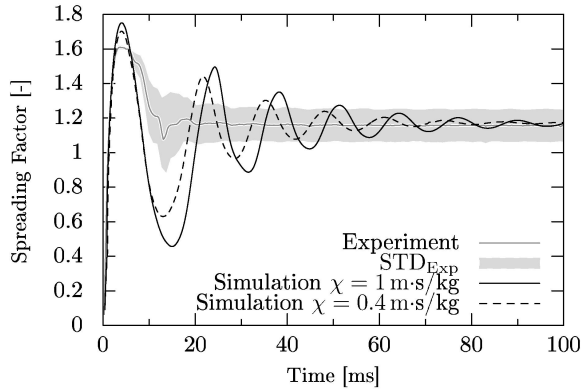


Figure 5: Spreading factor over time for the flat PDMS surface.

4.1. Spreading Factor

A suitable measure to quantify contact line dynamics is the spreading factor, defined as ratio between the diameter of the wetted area to the initial drop diameter D_0 . The time evolution of this dimensionless parameter allows to compare the experimental and numerical results quantitatively as shown in Fig. 5. The grey line labelled as experiment shows the spreading factor of the averaged 20 experiments. In the background of this line, the standard deviation is indicated as grey area (STD_{Exp}). The standard deviation reveals that with the start of the receding phase (8 ms), the uncertainty rises and keeps being rather high in the equilibrium state. This can be explained by the finite roughness of the PDMS surface. The corresponding microscopic irregularities act as barriers for the movement of the contact line. This causes the contact line to pin at different positions leading to a certain level of standard deviation even for the equilibrium state. Note that even nanometric defects may cause contact line pinning [35] and contact angle hysteresis [36].

Fig. 5 also shows the black solid line which corresponds to the simulation results with $\chi = 1 \text{ m}\cdot\text{s}/\text{kg}$ and $M = 4.84 \cdot 10^{-10} \text{ m}^3/\text{s}/\text{kg}$. The black dashed line shows the result of the simulation with $\chi = 0.413 \text{ m}\cdot\text{s}/\text{kg}$ and $M = 2 \cdot 10^{-10} \text{ m}^3/\text{s}/\text{kg}$. It can be clearly seen that the first advancing phase till about 6 ms shows very good agreement between experiment and numerics. The final equilibrium state for the spreading factor is also in excellent agreement. During the droplet oscillation phase, significant differences are observed. First, the plot reveals a higher peak for the maximum spreading factors in both simulations as well as earlier and more pronounced receding phases. In addition, the numerical results show clearly more oscillations before reaching an equilibrium state. This is plausible, since the flat surface in the sim-

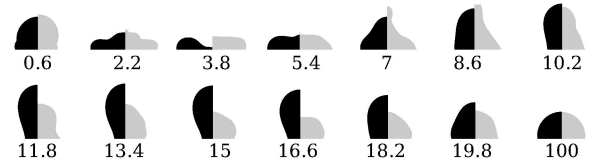


Figure 6: Drop shapes after impact on the flat surface over time (ms) in simulation (black) and experiment (grey). At 8.6 ms the grey drop is truncated at the top due to limited field of view in the experiment.

ulation is assumed perfectly smooth without any roughness and therefore is expected to cause a more dynamic behaviour. A decrease of the mobility leads to a reduction of the maximum spreading factor and subsequently a less dynamic spreading behaviour.

4.2. Instantaneous drop shape

For further validation, Fig. 6 compares the instantaneous droplet shapes in experiment and simulation. Each picture for the 14 different instances in time is divided into two parts. The grey colour on the right visualizes the experimental shape of one single experiment. The picture is acquired as described in Section 2 so the displayed shape is a lateral projection of the droplet. The black colour on the left corresponds to the simulation with mobility $M = 4.84 \cdot 10^{-10} \text{ m}^3/\text{s}/\text{kg}$. The shape of the droplet is extracted via the order parameter C being ≥ 0 . The picture shows the shape of the droplet as a vertical cross section through the mid-plane.

For the times 0.6, 2.2, 3.8 and 5.4 ms, the pictures are matching perfectly. The apparent difference at 3.8 ms can be explained by the mentioned different acquisition techniques. As the actual shape of the droplet at 3.8 ms has a rotational accumulation at the outside rim (see Fig. 6 left part), the projection from the side yields a uniform flat profile (see Fig. 6 right part).

At time 7 ms, the phase-field simulation can still reproduce the bulk shape recorded in the experiment but fails to capture the small jetting tip at the top of the droplet. With current resolution, the experimental tip radius corresponds to about eight mesh cells only. Clearly, this resolution is too less to capture the surface tension dominated tip region in the present simulation accurately. This failure is also related to the effect of interfacial relaxation which is inherent to the phase-field modelling as long as the system is out of equilibrium and an artificially thick interface is used [37].

The pictures for the period 8.6 – 19.8 ms show different shapes in experiment and simulation, which is also expected judging from Fig. 5. A closer look on the experimental images at 11.8 and 13.4 ms indicates

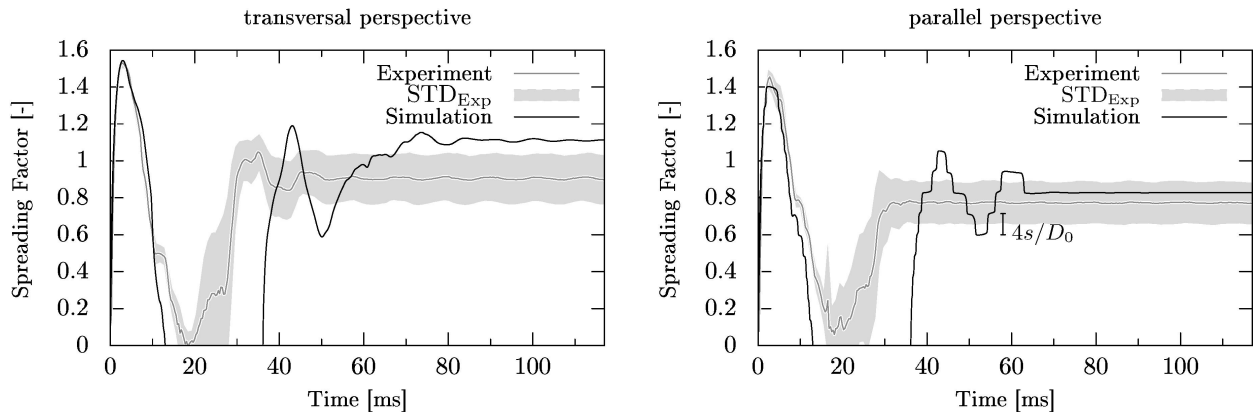


Figure 7: Spreading factor over time for the structured PDMS surface from two perspectives.

a distinct change of the drop shape close to the substrate with an alternation of the apparent contact angle from values smaller than 90° to values larger than 90° , associated with the reversal of the contact line motion from receding to advancing within this period. This rather abrupt reversal goes along with a lower peak in the averaged spreading factor (cf. Fig. 5), indicating that the process is reproducible. From 19.8 ms onwards, the spreading factor of the experiment remains constant, while the droplet shape itself is still changing. This indicates pinning of the contact line at the surface, possibly due to imperfections. In the simulation, no such abrupt changes of the drop shape are observed. At the equilibrium state (100 ms), nicely matching droplet shapes are obtained again in Fig. 6.

5. Results for drop impact on structured surface

5.1. Spreading Factor

Fig. 7 shows the spreading factor for the structured surface from transversal (left) and parallel (right) perspectives. Displayed in grey is the averaged experimental result along with its standard deviation and in black the result of the simulation. For the transversal perspective, experiment and simulation reveal a perfect match during the entire advancing phase and in the maximum spreading factor. Also, the beginnings of the receding curves are matching. From 10 ms onwards, the simulation curve and the averaged experimental curve start to differ from each other. The experimental graph reveals an almost constant value for 10 – 12 ms, indicating a temporal pinning of the droplet. During the same time interval, the contact line recedes in the simulation by about constant speed until a spreading factor of zero is reached indicating bouncing. The time interval between initial wall contact and drop bouncing is denoted

as contact time. Richard et al. [38] derived a correlation for the contact time of drops bouncing from flat superhydrophobic surfaces ($\theta_e > 150^\circ$). For the present drop, this correlation predicts a contact time of about 10.4 ms. This value is in a comparable range to the present values of 13 ms in the simulation and 15 ms in the experiment.

Both in experiment and simulation, the droplets detach from the surface. In the experiment, a tiny amount of water remains on the surface while the droplet is bouncing, cf. Fig. 8 at 18.2 ms. This leftover of water on the surface is the reason why the spreading factor of the experiment does not fully reach zero. One main difference between the simulation and the experiment is the residence time of the droplet in the air which is much shorter in the experiment. One plausible reason for this difference is the fact that the real surface in the experiment has the $60 \mu\text{m}$ groove structure, but also has additional roughness and defects. These imperfections lead to an additional barrier that has to be overcome during the dynamic process. As during the receding phase the droplets kinetic energy is already reduced as compared to the advancing phase, the receding contact line motion is more prone to a delay by these barriers. The additional energy that has to be invested to overcome imperfections leads to less remaining kinetic energy for the detaching droplet. Consequently, this leads to a difference in bouncing height, as will be later shown in Fig. 8. This difference in bouncing height goes along with different resident time of the droplet in the air. Further causes for that difference may be related to contact line boundary condition, surface tension modelling, interface thickness, mobility and groove resolution. However, we here are unable to investigate and quantify these effects.

Once the droplets impacts on the surface the second time, the advancing phase starts again. Due to less ki-

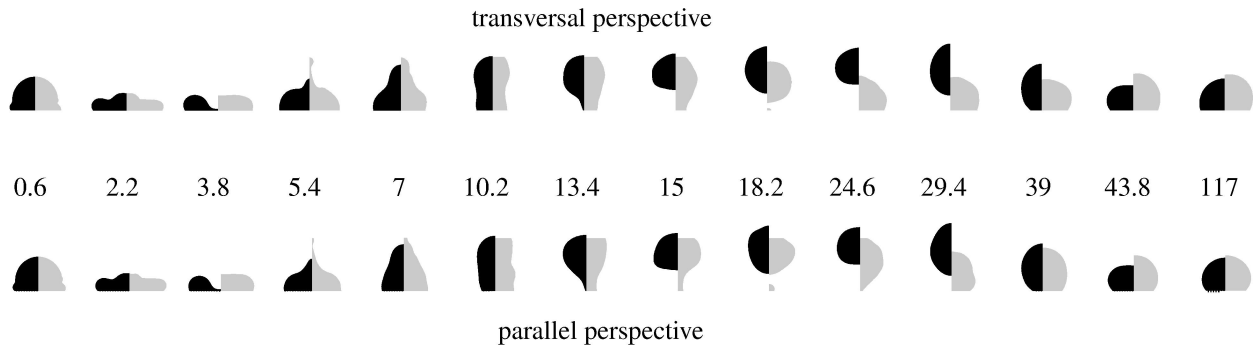


Figure 8: Drop shapes after impact on the structured surface over time (ms) in simulation (black) and experiment (grey) from transversal (top) and parallel (bottom) perspectives. Note that some of the grey drops are truncated at the top due to limited field of view in the experiment. For the transversal perspective, this concerns the pictures from 10.2 – 15 ms and, for the parallel perspective, the pictures from 7 - 24.6 ms.

netic energy present in the experiment, the maximum spreading factor of this second impact is not as high as in the simulation. Also, the second receding phase is more developed in the simulation. This reflects the behaviour from the previous receding phase. The major difference between simulation and experiment is the equilibrium state at the end. Here, the simulation does not match the value of the experiment within the standard derivation.

The temporal evolution of the spreading factor from the parallel perspective is displayed on the right side of Fig. 7. The advancing phase and the maximum values of the spreading factor show again very good agreement. For the receding phase, a very small shift in time can clearly be seen: the receding phase of the experiment starts a bit later. This shift is permanently seen and becomes larger until the droplet detaches from the surface. This growth in the time shift is in accordance with the idea that in the experiment, a higher energy barrier has to be overcome during receding. Once the two droplets have impacted on the surfaces, again they reveal different behaviour. While in the averaged experimental curve, the final value of the spreading factor has already been reached after one advancing phase after rebound, in the simulation the behaviour is more dynamic.

Especially noticeable is the stepwise change of the numerical spreading factor for the parallel perspective displayed in Fig. 7. In the corresponding averaged experimental curve, no stepwise change can be observed. The steps in the numerical results are particularly clear in the period 40 – 65 ms when the rapid change of the spreading factor following the second impact after bouncing has slowed down and the energy barrier to wet/dewet a groove cannot be overcome instantaneously. The step width of 4s in the numerical curve corresponds to the wetting/dewetting of one periodicity

length of the surface structure ($2s$) on both sides of the drop. The pinning process at the grooves is visualized in a video provided as supplementary material. By visualizing the temporal evolution of the gas-liquid interface, the pinning at the edges of the grooves is identified. It reveals that wetting and dewetting happen almost simultaneously over the groove and the ridge between neighbouring grooves.

Similar to the transversal perspective, the terminal spreading factor in parallel direction is larger in the simulation as compared to the experiment. The difference in the parallel perspective is, however, much smaller and equivalent to a distance of about 60 μm . The systematic larger terminal spreading factors in the simulation are related to the lower terminal drop height, cf. the discussion at the end of Section 5.2.

5.2. Instantaneous drop shape

Fig. 8 shows selected shapes of the impacting droplet over time. As before, the numerical results are visualized in black and the corresponding experimental results in grey. On the structured surface the two different perspectives indicated in Fig. 2 are considered. While both perspectives are extracted from one simulation run, the experimental results are obtained in two consecutive experiments, i.e., from different drops.

The first three instants of time (0.6, 2.2 and 3.8 ms) show very good agreement between experiment and simulation and indicate no visible difference between the two different perspectives. The apparent difference in experimental/computed droplet shape at 3.8 ms originates from the different recording techniques as explained in Section 4.2. Also, the reason for the difference in drop shapes at time 5.4 ms (where the experiment shows a jet which is much less pronounced in the simulation) is discussed in Section 4.2 already. At

this instant in time, the shapes in the bottom part show very good agreement between experimental and numerical results in each perspective while first differences between the two different perspectives become visible. While the shape in the transversal perspective is rather bulbous (in the lower part of the droplet), the parallel perspective reveals a more conical shape. This happens because the drop can evolve freely in the transversal direction, while the grooves restrict its motion in parallel direction.

For the times 7 and 10.2 ms, experiment and simulation show very similar droplet shapes while differences between the respective directions are clearly present. From time 13.4 ms onwards, obvious differences between experiment and simulation are found. They mainly originate from differences in contact time and bouncing time, as already discussed in Section 5.1. The droplet shapes at 10.2 and 13.4 ms visualise nicely the different dynamics of the receding contact line in that period. While the decrease of the wetted surface area visible in the black simulated droplet shapes is very large, it is much smaller for the grey experimental droplet shapes. These observations are in correspondence with the less quickly decreasing spreading factor and longer contact time in the experiment as compared to the simulation (cf. Fig. 7).

For the black simulation droplet at time 13.4 ms, the drop's shapes still reveal perspective differences, even though the contact to the surface is minimized. As the droplet maintains the change in shape up to this point, it is logical to see this difference also during the rebounding phase. During the rebounding phase, the main two aspects that disagree between the experiment and the simulation are the bouncing height of the droplet (consequently also its residence time in the air) and the tiny amount of water staying on the surface in the experiment versus the complete rebound of the droplet in the simulation.

For the final stage, Fig. 8 reveals that the terminal drop height in the simulation is lower than in the experiment, while the experimental values in both perspectives differ as well. The terminal drop height above the ridges is 1.519 mm in the simulation while the corresponding experimental values in transversal and parallel perspective are 1.635 mm and 1.586 mm, respectively. Since the drop volume in experiment and simulation is the same, the 5 – 7% lower terminal numerical drop height corresponds to larger values of the terminal numerical spreading factor in both directions, cf. Fig. 7.

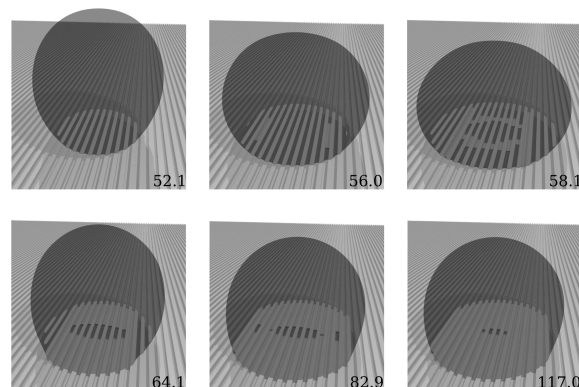


Figure 9: Simulation results illustrating the evolution of the wetting state of the grooves over time (ms).

5.3. Air entrapment within the grooves

When the water droplet impacts on the structured surface the grooves can either be filled with water (Wenzel state) or can enclose entrapped air (Cassie state). The actual condition of the grooves can only be analysed in the simulation but not by the experiment due to reduced optical accessibility.

During the initial impact on the surface, the grooves are not wetted. When the droplet impacts the surface a second time after bouncing, the grooves are slowly, one by one, filled with water. Fig. 9 shows the evolution of the condition of the grooves over time. The first picture (52.1 ms) reveals the drop sitting on the surface without water wetting the grooves: when water wets the surface the visualisation colour of the solid-liquid interface is grey; when water has a liquid-gas interface the visualisation colour is darker. At 52.1 ms the picture reveals the ridges between the grooves being wetted, but the grooves themselves are not wetted. On the picture at 56 ms two grooves begin to wet. As described in Section 3.2.5, the simulation resolves a quarter of the droplet. This necessitates the symmetric behaviour of the droplet. At 58.1 ms, the same two grooves are completely wetted. Additionally, the picture reveals a circular wetting pattern on the grooves which evolves until 64.1 ms and wets the complete grooves towards the outer boundaries of the droplet while the inner part of these grooves still encloses entrapped air.

The picture for 82.9 ms shows all grooves being partially or fully wetted. From this point on, the observed behaviour is not physical any longer as air seems to diffuse out of the grooves. This can be explained considering the numerical parameters of the simulation. As stated in Section 3.2.3, the Cahn number is based on a characteristic length scale. Here, the drop diameter

is taken for that purpose as obvious choice for drop impact phenomena. However, in order to capture the evolution of the entrapped air properly, the underlying characteristic length scale should be the groove width. Clearly, the Cahn number based on the groove length scale $\varepsilon/s = 0.36$ is much too high to simulate the air entrapment inside the grooves accurately.

6. Summary and conclusions

From the present experimental and computational study with a phase-field method, several conclusions can be drawn. In the experiment with the structured surface, a good reproducibility is obtained for the inertia dominated expanding phase towards the maximum spreading diameter as well as for the subsequent receding phase till bouncing. For the flat surface, the reproducibility is good for the spreading phase and the beginning of the receding phase. For these stages, the corresponding computational spreading factors and instantaneous drop shapes on both substrates are in reasonable good agreement with measured data.

After the deterministic phase discussed above, much larger standard deviations are obtained for the time evolution of the experimental spreading factor on both substrates indicating limited reproducibility. The corresponding variations can be attributed to temporal or permanent pinning effects caused by microscopic surface imperfections associated with finite roughness. In the numerical results for the perfectly smooth flat surface without any roughness, no pinning effects are observed, as expected. For the structured surface, temporal pinning is observed in the simulation, which is well correlated to the periodicity length of the micro-grooves. Overall, the microscopic roughness effects present in the experiment and absent in the simulations cause a more dynamic behaviour of the wetted surface area and less dynamic behaviour of the gas-liquid interface in the simulations as compared to the experiment.

Concerning the wetted surface area in the final static state, good agreement between computational and averaged experimental results is obtained on the flat substrate. On the structured surface, the terminal spreading factors in both perspectives are larger in the simulation as compared to the experiment, corresponding with a smaller terminal droplet height.

Overall, the agreement between simulation and experiment in terms of spreading factor and instantaneous drop shape is good for the inertia-driven advancing (spreading) phases of drop motion. The subsequent receding phases are more dominated by surface tension and contact line dynamics. There, the agreement is good

for the flat surface only at the very beginning and for the structured surface somewhat longer. For the subsequent oscillation phase (flat surface) and bouncing phase (structured surface), the differences in spreading factor and drop shape are large. While the proposed phase-field method can thus not correctly reproduce the entire liquid motion, it is remarkable that it correctly recovers the experimentally observed outcomes of the drop impingement, namely deposition without rebound on the flat surface and bouncing on the micro-grooved surface. The duration of the rebound in the simulation is larger than in the experiment, where microscopic surface roughness dissipates more energy during drop recoil. Nevertheless, reproducing the distinct experimental droplet impingement outcomes on both surfaces is notable since it is obtained using the same static contact angle in the wetting boundary condition and identical values for capillary width, mobility and grid resolution. So far the present study is limited to one combination of drop diameter and impact velocity only, which is of course insufficient for a thorough validation concerning impingement outcomes. The results nevertheless indicate the large potential of the phase-field method for correctly predicting drop bouncing phenomena.

The simulation results on the structured surface encompass the wetting/dewetting behaviour within the grooves including air entrapment, however at insufficient resolution. This reveals challenges to future work where, for adequate resolution of these phenomena, adaptive mesh refinement should be employed.

Acknowledgement

This work was performed on the computational resources bwUniCluster and ForHLR Phase II funded by the Ministry of Science, Research and the Arts Baden-Württemberg and DFG ('Deutsche Forschungsgemeinschaft') within the framework program bwHPC. Further DFG support is acknowledged by VF and BF through project FR2823/2-1 and by HM through Collaborative Research Centre 1194, Project B02. XC acknowledges financial support by DFG through SFB/TRR 150, project B05. We acknowledge T. Rajabi, K. Simon, R. Tuschen and M. Weinbuch for support in the experimental campaign. Finally, we thank the reviewers for their useful comments.

Supplementary materials

Supplementary video material and data for Fig. 5 and Fig. 7 can be found, in the online version, at doi:10.1016/j.ijheatfluidflow.2018.02.014.

References

References

- [1] A. Worthington, On the forms assumed by drops of liquids falling vertically on a horizontal plate, *P. R. Soc. London* 25 (1876) 261–272.
- [2] A. L. Yarin, Drop impact dynamics: Splashing, spreading, receding, bouncing ..., *Annu. Rev. Fluid Mech.* 38 (2006) 159–192.
- [3] C. Josserand, S. Thoroddsen, Drop impact on a solid surface, *Annu. Rev. Fluid Mech.* 48 (2016) 365–391.
- [4] J. P. Davim, M. J. Jackson, *Nano and Micromachining*, Wiley, 2008.
- [5] D. Quéré, Wetting and roughness, *Ann. Rev. Mat. Res.* 38 (2008) 71–99.
- [6] R. J. Crawford, E. P. Ivanova, *Superhydrophobic Surfaces*, Elsevier, 2015.
- [7] D. Khojasteh, M. Kazerooni, S. Salarian, R. Kamali, Droplet impact on superhydrophobic surfaces: A review of recent developments, *J. Ind. Eng. Chem.* 42 (2016) 1–14.
- [8] K. Range, F. Feuillebois, Influence of surface roughness on liquid drop impact, *J. Colloid Interf. Sci.* 203 (1998) 16–30.
- [9] V. Vaikuntanathan, D. Sivakumar, Maximum spreading of liquid drops impacting on groove-textured surfaces: Effect of surface texture, *Langmuir* 32 (2016) 2399–2409.
- [10] L. K. Malla, N. D. Patil, R. Bhardwaj, A. Neild, Droplet bouncing and breakup during impact on a microgrooved surface, *Langmuir* 33 (2017) 9620–9631.
- [11] R. Kannan, D. Sivakumar, Drop impact process on a hydrophobic grooved surface, *Colloids Surf., A* 317 (2008) 694–704.
- [12] H. Kim, U. Park, C. Lee, H. Kim, M. H. Kim, J. Kim, Drop splashing on a rough surface: How surface morphology affects splashing threshold, *Appl. Phys. Lett.* 104 (2014) 161608.
- [13] D. Richard, D. Quéré, Bouncing water drops, *EPL - Europhys. Lett.* 50 (2000) 769–775.
- [14] Y. C. Jung, B. Bhushan, Dynamic effects of bouncing water droplets on superhydrophobic surfaces, *Langmuir* 24 (2008) 6262–6269.
- [15] L. Moevius, Y. Liu, Z. Wang, J. M. Yeomans, Pancake bouncing: Simulations and theory and experimental verification, *Langmuir* 30 (2014) 13021–13032.
- [16] A. Yagub, H. Farhat, S. Kondaraju, T. Singh, A lattice Boltzmann model for substrates with regularly structured surface roughness, *J. Comput. Phys.* 301 (2015) 402–414.
- [17] J. Wang, M. Do-Quang, J. J. Cannon, F. Yue, Y. Suzuki, G. Amberg, J. Shiomi, Surface structure determines dynamic wetting, *Scientific Reports* 5 (2015) 8474.
- [18] Y. Wang, S. Chen, Droplets impact on textured surfaces: Mesoscopic simulation of spreading dynamics, *Appl. Surf. Sci.* 327 (2015) 159–167.
- [19] L. Wang, R. Zhang, X. Zhang, P. Hao, Numerical simulation of droplet impact on textured surfaces in a hybrid state, *Microfluid. Nanofluid.* 21 (2017) 61.
- [20] H. Tan, Numerical study on splashing of high-speed microdroplet impact on dry microstructured surfaces, *Comput. Fluids* 154 (2017) 142–166.
- [21] A. M. Moqaddam, S. S. Chikatamarla, I. V. Karlin, Drops bouncing off macro-textured superhydrophobic surfaces, *J. Fluid Mech.* 824 (2017) 866–885.
- [22] C. Tropea, A. L. Yarin, *Springer handbook of experimental fluid mechanics*, Vol. 1, Springer Science & Business Media, 2007.
- [23] D. M. Anderson, G. B. McFadden, A. A. Wheeler, Diffuse-interface methods in fluid mechanics, *Annu. Rev. Fluid Mech.* 30 (1998) 139–165.
- [24] D. Jacqmin, Calculation of two-phase Navier–Stokes flows using phase-field modeling, *J. Comput. Phys.* 155 (1999) 96–127.
- [25] F. Bai, X. He, X. Yang, R. Zhou, C. Wang, Three dimensional phase-field investigation of droplet formation in microfluidic flow focusing devices with experimental validation, *Int. J. Multiph. Flow* 93 (2017) 130–141.
- [26] X. Cai, H. Marschall, M. Wörner, O. Deutschmann, Numerical simulation of wetting phenomena with a phase-field method using OpenFOAM®, *Chem. Eng. Technol.* 38 (2015) 1985–1992.
- [27] X. Cai, Interface-resolving simulations of gas-liquid two-phase flows in solid structures of different wettability, Ph.D. thesis, Karlsruhe Institut für Technologie (KIT), Karlsruhe (2016).
- [28] X. Cai, M. Wörner, H. Marschall, O. Deutschmann, Numerical study on the wettability dependent interaction of a rising bubble with a periodic open cellular structure, *Catal. Today* 273 (2016) 151–160.
- [29] X. Cai, M. Wörner, H. Marschall, O. Deutschmann, CFD simulation of liquid back suction and gas bubble formation in a circular tube with sudden or gradual expansion, *Emiss. Contr. Sci. Technol.* 3 (2017) 289–301.
- [30] R. G. Cox, The dynamics of the spreading of liquids on a solid surface. Part 1. Viscous flow, *J. Fluid Mech.* 168 (1986) 169–194.
- [31] P. Yue, C. Zhou, J. J. Feng, Sharp-interface limit of the Cahn–Hilliard model for moving contact lines, *J. Fluid Mech.* 645 (2010) 279–294.
- [32] H. Kusumaatmaja, E. J. Hemingway, S. M. Fielding, Moving contact line dynamics: from diffuse to sharp interfaces, *J. Fluid Mech.* 788 (2016) 209–227.
- [33] R. Bernard, Phasensfeld Simulationen eines Tropfenauflaufpralls auf strukturierten Oberflächen, Master’s thesis, Karlsruhe Institute of Technology (KIT), Karlsruhe, Germany (2016). doi:10.5445/IR/1000079086.
- [34] P. G. Bange, R. Bhardwaj, Computational study of bouncing and non-bouncing droplets impacting on superhydrophobic surfaces, *Theor. Comput. Fluid Dyn.* 30 (2016) 211–235.
- [35] T. Ondarçuhu, A. Piednoir, Pinning of a contact line on nanometric steps during the dewetting of a terraced substrate, *Nano Letters* 5 (2005) 1744–1750.
- [36] M. Delmas, M. Monthieux, T. Ondarçuhu, Contact angle hysteresis at the nanometer scale, *Phys. Rev. Lett.* 106 (2011) 136102.
- [37] P. Yue, J. J. Feng, C. Liu, J. Shen, A diffuse-interface method for simulating two-phase flows of complex fluids, *J. Fluid Mech.* 515 (2004) 293–317.
- [38] D. Richard, C. Clanet, D. Quéré, Surface phenomena: Contact time of a bouncing drop, *Nature* 417 (6891) (2002) 811–811.